

The Orbital Evolution Induced by Baryonic Condensation in Triaxial Halos

Monica Valluri^{1*}, Victor P. Debattista², Thomas Quinn³, Ben Moore⁴

¹ *Department of Astronomy, University of Michigan, Ann Arbor, MI 48109, USA*

² *RCUK Fellow; Jeremiah Horrocks Institute for Astrophysics and Supercomputing, University of Central Lancashire, Preston, PR1 2HE, UK*

³ *Astronomy Department, University of Washington, Box 351580, Seattle, WA 98195-1580, USA*

⁴ *Department of Theoretical Physics, University of Zürich, Winterthurerstrasse 190, CH-8057, Zürich, Switzerland*

29 May 2019

ABSTRACT

Using spectral methods, we analyse the orbital structure of dark matter (DM) in N -body simulations in an effort to understand the physical processes that drive the evolution of dark matter halo shapes caused by growing central masses. A longstanding issue is whether the change in the shapes of DM halos is the result of chaotic scattering of the major family of box orbits that serves as the back-bone of a triaxial system, or whether they change shape in response to the evolving galactic potential. We use the characteristic orbital frequencies to classify orbits into major orbital families, to quantify orbital shapes, and to identify resonant orbits and chaotic orbits. We show that regardless of the distribution of the baryonic component, the shape of a DM halo changes primarily due to changes in the shapes of individual orbits within a given family. Orbits with small pericentric radii are more likely to change both their orbital type and shape than orbits with large pericentric radii. Whether the evolution is regular (and reversible) or chaotic (and irreversible), depends primarily on the radial distribution of the baryonic component. A massive, compact central mass results in chaotic scattering of a large enough fraction of both box and long-axis tube orbits, even at fairly large pericentric distances, such that the evolution is not reversible. Frequency maps show that the growth of a disk causes a significant fraction of halo particles to become associated with major global orbital resonances.

1 INTRODUCTION

The condensation of baryons to the centres of dark matter halos leads to the halos becoming more spherical or axisymmetric (Dubinski 1994; Kazantzidis et al. 2004; Debattista et al. 2008, hereafter D08). D08 found that the halo shape changes by $\Delta(b/a) \gtrsim 0.2$ out to at least half the virial radius. This shape change reconciles the strongly prolate-triaxial shapes found in collisionless N -body simulations of the hierarchal growth of halos (Bardeen et al. 1986; Barnes & Efstathiou 1987; Frenk et al. 1988; Dubinski & Carlberg 1991; Jing & Suto 2002; Bailin & Steinmetz 2005; Allgood et al. 2006) with observations, which generally find much rounder halos (Schweizer et al. 1983; Sackett & Sparke 1990; Iodice et al. 2003; Buote & Canizares 1994; Buote et al. 2002; Diehl & Statler 2007; Olling 1995,

1996; Olling & Merrifield 2000; Banerjee & Jog 2008; Kochanek 1995; Bartelmann et al. 1995; Koopmans et al. 1998; Oguri et al. 2003; Franx & de Zeeuw 1992; Huizinga & van Albada 1992; Kuijken & Tremaine 1994; Franx et al. 1994; Schoenmakers et al. 1997; Andersen et al. 2001; Debattista 2003; Barnes & Sellwood 2003).

What is the physical mechanism driving shape change? Options suggested in the literature include two possibilities. The first is that the presence of a central mass concentration scatters box orbits that serve as the backbone of a triaxial potential, rendering them chaotic (Gerhard & Binney 1985; Merritt & Valluri 1996; Merritt & Quinlan 1998). Once orbits become chaotic, they are free to diffuse over the entire energy surface, which is in general rounder than the density distribution. This diffusion or “chaotic mixing”

causes the potential to evolve to a more oblate or even a spherical distribution. The second possibility is that the change of the central potential occurs because the growth of the baryonic component causes orbits of collisionless particles in the halo to respond by changing their shapes in a regular (and therefore reversible) manner (Holley-Bockelmann et al. 2002).

One of the principal features of chaotic evolution is irreversibility. This irreversibility arises from two properties of chaotic orbits. First, chaotic orbits are exponentially sensitive to small changes in initial conditions even in a collisionless system. Second, chaotic systems display the property of *chaotic mixing* (Lichtenberg & Lieberman 1992). Using this principle of irreversibility, D08 argued that if chaotic evolution is the primary driver of shape change, then if, subsequently, the central mass concentration is artificially “evaporated”, the system would not be able to revert to its original triaxial distribution. D08 showed that growing baryonic components inside prolate/triaxial halos led to a large change in the shape of the halo. Despite these large changes, by artificially evaporating the baryons, they showed that the underlying halo phase space distribution is not grossly altered unless the baryonic component is too massive or centrally concentrated, or transfers significant angular momentum to the halo. This led them to argue that chaotic evolution alone cannot explain the shape change since such a process is irreversible. They speculated that at most only slowly diffusive chaos occurred in their simulations. Using test particle orbit integrations they also showed that box orbits largely become deformed, possibly changing into loop orbits, during disk growth, but do not become strongly chaotic.

D08 employed irreversibility as a convenient proxy for the presence of chaos. In this paper we now undertake an orbital analysis of some of the models studied by D08 to better understand the mechanism that drives shape change. Our goal is to address the following questions: (a) are chaotic orbits an important driver of shape change and if so under what conditions are they important? (b) how do the orbital populations in halos change when a centrally concentrated baryonic component grows inside a triaxial dark matter halo? (c) what factors determine whether orbits change their orbital classification from one configuration to another?

This paper is organised as follows. In § 2 we describe the simulations used in this paper and briefly review the results on these specific models from D08 as well as one new additional simulation. In § 3 we describe the principal technique: Numerical Analysis of Fundamental Frequencies (NAFF) that we use to obtain frequency spectra and fundamental frequencies and describe how these frequencies are used to characterise orbits. In § 4 we describe the results of our analysis of four different simulations. In § 5 we discuss our results and present our conclusions.

2 NUMERICAL SIMULATIONS

We formed prolate/triaxial halos via mergers of systems, as described in Moore et al. (2004). The initially spherical NFW

(Navarro et al. 1996) halos were generated from a distribution function using the method described in Kazantzidis et al. (2004) with each halo composed of two mass species arranged on shells. The outer shell has more massive particles than the inner one. Our model halo A was generated by the head-on merger of two prolate halos, themselves the product of a binary merger of spherical systems. The first merger placed the concentration $c = 10$ halos 800 kpc apart approaching each other at 50 km s^{-1} , while the second merger starts with the remnant at rest, 400 kpc from an identical copy. The resulting halo is highly prolate with a mild triaxiality. Halo model B was produced by the merger of two spherical halos starting at rest, 800 kpc apart and is prolate, with $\langle b/a \rangle = \langle c/a \rangle \simeq 0.58$. Halo A has $\langle b/a \rangle \simeq 0.45$ and $\langle c/a \rangle \simeq 0.35$ while halo B has $\langle b/a \rangle = \langle c/a \rangle \simeq 0.58$ (see Figure 3 of D08 for more details). Both halos A and B consist of 4×10^6 particles. The outer particles are ~ 18 times more massive in halo A and ~ 5 times more massive in halo B. A large part of the segregation by particle mass persists after the mergers and the small radius regions are dominated by low mass particles (cf. Dehnen 2005). We used a softening parameter $\epsilon = 0.1 \text{ kpc}$ for all halo particles.

Once we produced the prolate/triaxial halos, we inserted a baryonic component, either a disk of particles that remains rigid throughout the experiments or softened point particles. Initially, the disk has negligible mass, but this grows adiabatically linearly over time to a mass M_b during a time t_g . After this time, we slowly evaporated it during a time t_e . We stress that this evaporation is a numerical convenience for testing the effect of chaos on the system, and should not be mistaken for a physical evolution. The disk is composed of 300K equal-mass particles each with a softening $\epsilon = 100 \text{ pc}$. The disk was placed with its symmetry axis along the halo’s short in model SA1 (additional orientations of the disk relative to the principal axes were also simulated but their discussion is deferred to a future paper). The density distribution of the disk was exponential with scale length R_d and Gaussian scale-height $z_d/R_d = 0.05$. From $t = 0$ to $t_g + t_e$ the halo particles are free to move and achieve equilibrium with the baryons as their mass changes, but all disk particles are frozen in place. We also ran experiments with a softened particle instead of a disk, with its mass grown in the same way (models P_fA3, P_fB2, P_fB3). We refer to these experiments by the label “P” subscripted by “f” for particles frozen in place and by “l” for live particles free to move. D08 showed that there is no significant difference in the evolution between pairs of simulations with frozen versus live central particles, all other things being equal. The baryonic component in these simulations are meant to loosely represent either the stellar distribution of an elliptical galaxy or a massive, compact bulge, depending on the softening adopted.

Models SA1, P_fB2, and P_fB3 have been described previously in D08, where the same naming convention is used. P_fA3 is new to this paper. It was constructed in order to have a model with a spherical baryonic distribution which can be contrasted with model SA1.

| Run | Halo | r_{200} [kpc] | M_{200} [$10^{12}M_{\odot}$] | M_b [$10^{11}M_{\odot}$] | f_b | R_d [kpc] | t_g [Gyr] | t_e [Gyr] |
|-------------------|------|--------------------|-------------------------------------|---------------------------------|-------|----------------|----------------|----------------|
| SA1 | A | 215 | 4.5 | 1.75 | 0.039 | 3.0 | 5 | 2.5 |
| P _l A3 | A | 215 | 4.5 | 1.75 | 0.039 | 1.0 | 5 | 2.5 |
| P _f B2 | B | 106 | 0.65 | 0.7 | 0.108 | 3.0 | 10 | 4 |
| P _l B3 | B | 106 | 0.65 | 0.35 | 0.054 | 0.1 | 5 | 5 |

Table 1. The simulations in this paper. M_b is the mass in baryons and f_b is the baryonic mass fraction. For the particle simulations (P_fB2, P_lB3, P_lA3), R_d refers to the softening of the spherical baryonic distribution particle(s). For simulation SA1, R_d refers to the disk scale length.

For each model, the initial phase without the baryonic component is referred to as *phase a*. When the baryonic component has finished growing to full strength, the model is referred to as being in *phase b*. The final phase of evolution after the baryonic component has been adiabatically evaporated is referred to as *phase c*.

All the simulations in this paper, which are listed in Table 1, were evolved with PKDGRAV (Stadel 2001), an efficient, multi-stepping, parallel treecode. We used an opening angle of $\theta = 0.7$ throughout. Further details of the simulations can be found in D08.

2.1 Computing Orbits

In each of the halos studied we selected a subsample of between 1000-6000 particles and followed their orbits at various points in the simulation. The particles were randomly chosen in the halos at $t = 0$ such that they were inside a fixed outer radius (either 100 or 200 kpc.) We then integrated their motion as test particles while holding all the other particles fixed in place. We used a fixed timestep of 0.1 Myr and integrated for 50 Gyr, storing the phase space coordinates of each test particle every 1 Myr. We used such long integration times to ensure we are able to obtain accurate measurements of frequencies (as described in the next section). We carried out this operation for the same subset of particles at *phases a*, *b* and *c*. In model SA1 (baryonic disk with symmetry axis parallel to short axis) we integrated the orbits of 6000 particles which in *phase a* were within $r = 200$ kpc. In model P_lA3 we considered a subsample of 5000 particles starting within $r = 100$ kpc. In models P_fB2 and P_lB3 we considered orbits of 1000 particles within $r = 200$ kpc. We integrated their orbits as above but we used a smaller timestep $\delta t = 10^4$ years in the case of P_lB3. The orbit code computes forces based on the PKDGRAV tree; we used the same $\theta = 0.7$ for the orbit calculations.

3 FREQUENCY ANALYSIS

In a galactic potential that is close to integrable, all orbits are quasi-periodic. If an orbit is quasi-periodic (or regular), then any of its

coordinates can be described explicitly as a series,

$$x(t) = \sum_{k=1}^{\infty} A_k e^{i\omega_k t}, \tag{1}$$

where the ω_k 's are the oscillation frequencies and the A_k 's are the corresponding amplitudes. In a three dimensional system, each ω_k can be written as an integer linear combination of three fundamental frequencies $\omega_1, \omega_2, \omega_3$ (one for each degree of freedom). If each component of the motion of a particle in the system (e.g. $x(t)$) is followed for several (~ 100) dynamical times, a Fourier transform of the trajectory yields a spectrum with discrete peaks. The locations of the peaks correspond to the ω_k and their amplitudes A_k can be used to compute the linearly independent fundamental frequencies (Boozer 1982; Kuo-Petravic et al. 1983).

Binney & Spergel (1982, 1984) applied this method to galactic potentials and obtained the frequency spectra using a least squares technique to measure the frequencies ω_k . Laskar (1990, 1993) developed a significantly improved numerical technique (Numerical Analysis of Fundamental Frequencies, hereafter NAFF) to decompose a complex time series of the phase space trajectory of an orbit of the form $x(t) + iv_x(t)$, (where v_x is the velocity along the x coordinate). Valluri & Merritt (1998) developed their own implementation of this algorithm that uses integer programming to obtain the fundamental frequencies from the frequency spectrum. In this paper we use this latter implementation of the NAFF method.

We refer readers to the above papers for a detailed description of the method but provide a brief summary here. The NAFF algorithm for frequency analysis allows one to quickly and accurately compute the fundamental frequencies that characterise the quasi-periodic motion of regular orbits. The entire phase space at a given energy can then be represented by a frequency map which is a plot of ratios of the fundamental frequencies of motion. A frequency map is one of the easiest ways to identify families of orbits that correspond to resonances between the three degrees of freedom. The resonances that are most important for determining the structure of phase space appear as straight lines in the frequency map. The strength of the resonances change as the potential deviates from integrability in response to a perturbation. As the phase space occupied by resonances grows the phase space becomes more

and more chaotic. The strength of the resonances can be determined by the number of orbits that are associated with them.

3.1 Accuracy of frequency estimation

Frequency analysis can be used to distinguish between regular and chaotic orbits. In realistic galactic potentials most chaotic orbits are expected to be weakly chaotic and lie close to regular orbits mimicking their behaviour for long times. The rate at which weakly chaotic orbits change their orbital frequencies can be used as a measure of chaos. Laskar (1993) showed that the change in the fundamental frequencies over two consecutive time intervals can be used as a measure of the stochasticity of an orbit. This method has been used to study the phase space structure in galactic potentials (Papaphilippou & Laskar 1996, 1998; Valluri & Merritt 1998). For each time series the spectrum is analysed and the three fundamental frequencies are obtained. In Cartesian coordinates the frequencies would be $\omega_x, \omega_y, \omega_z$.

For each orbit we therefore divide the 50 Gyr time interval into two consecutive segments and use NAFF to compute the fundamental frequencies $\omega_x, \omega_y, \omega_z$ (note that all frequencies in this paper are in units of Gyr^{-1} and are hence not explicitly specified everywhere). We define ω_1 and ω_2 to be the largest fundamental frequencies obtained in the first and second time intervals respectively. We define a “frequency drift parameter”:

$$\log(\Delta f) = \log \left| \frac{\omega_1 - \omega_2}{\omega_1} \right|. \quad (2)$$

The larger the value of the frequency drift parameter, the more chaotic the orbit.

Distinguishing chaos however also requires that we properly account for numerical noise. In previous studies orbits were integrated with high numerical precision for at least 100 orbital periods, resulting in highly accurate frequency determination. For instance, Valluri & Merritt (1998) found that orbital frequencies in a triaxial potential could be recovered with an accuracy of 10^{-10} for regular orbits and $10^{-4} - 10^{-6}$ for stochastic orbits using integration times of at least 50 orbital periods per orbit¹. In N -body systems like those considered in this paper, the galactic mass distribution is realised as a discrete set of point masses. The discretization of the potential results in exponential deviation of nearby orbits, even in systems where all orbits are expected to be regular (Miller 1964; Goodman et al. 1993; Kandrup & Smith 1991; Valluri & Merritt 2000; Hemsendorf & Merritt 2002). However as the number of particles in a simulation is increased, and when point masses are softened, the majority of orbits appear very regular despite the fact that they have a non-zero Lyapunov exponent (which

saturates at a finite value beyond a few hundred particles). Thus despite being formally chaotic these orbits behave much like regular orbits (Kandrup & Sideris 2001; Kandrup & Siopis 2003).

In order to use frequency analysis to characterise orbits as regular or chaotic in N -body systems, it is necessary to assess the numerical accuracy of orbital frequencies obtained by the NAFF code. To quantify the magnitude of frequency drift that arises purely from discretization effects we select a system that is spherically symmetric and in dynamical equilibrium. All orbits in a smooth spherically symmetrical potential are rosettes confined to a single plane (Binney & Tremaine 1987) and are regular. Hence any drift in orbital frequencies can be attributed entirely to discretization errors (including minute deviations of the N -body potential from perfect sphericity). As a test of our application of the NAFF code to N -body potentials we analyse orbits in spherical NFW halos of two different concentrations ($c = 10$ and $c = 20$). The halos are represented by 10^6 particles and have mass $\sim 2 \times 10^{12} M_\odot$. Particles in both cases come in two species with softening of 0.1 kpc and 0.5 kpc. We carried out the frequency analysis of 1000 randomly selected orbits which were integrated for 50 Gyr in the frozen N -body realisations of each of the NFW halos.

Figure 1 shows the distribution of values of $\log(\Delta f)$ for both halos. In both cases the distribution has a mean value of $\log(\Delta f) = -2.29$, with standard deviations of 0.58 (for the $c = 10$ halo) and 0.54 (for the $c = 20$ halo). Both distributions are significantly skewed toward small values of $\log(\Delta f)$ (skewness = -0.85) and are more peaky than Gaussian (kurtosis = 1.95). Despite the fact that the two NFW halos have different concentrations, the distributions of $\log(\Delta f)$ are almost identical indicating that our chaotic measure is largely independent of the central concentration.

To define a threshold value of $\log(\Delta f)$ at which orbits are classified as chaotic we note that 99.5% of the orbits have values of $\log(\Delta f) < -1.0$. Since all orbits in a stationary spherical halo are expected to be regular, we attribute all larger values of $\log(\Delta f)$ to numerical noise arising from the discretization of the potential. Henceforth, we classify an orbit in our N -body simulations to be regular if it has $\log(\Delta f) < -1.0$.

To accurately measure the frequency of an orbit it is necessary to sample a significant part of its phase-space structure (i.e. the surface of a 2-torus in a spherical potential or the surface of the 3-torus in a triaxial potential). Valluri & Merritt (1998) showed that the accuracy of the frequency analysis decreases significantly when orbits integrated for less than 20 oscillation periods. Inaccurate frequency determination could result in misclassifying orbits as chaotic (since inaccurate frequency measurement can also lead to larger frequency drifts). We test the dependence of $\log(\Delta f)$ on the number of orbital periods n_p for which an orbit is integrated by plotting the frequency drift parameter against the largest orbital frequency (for orbits with $n_p > 20$) in both NFW halos in Figure 2². We use ω instead of n_p since $n_p \propto \omega$ but is harder to compute

¹ Valluri & Merritt (1998) used units in which $G = 1$, the total mass of the Dehnen model $M_{tot} = 1$, and semi-major axis $a = 1$.

² We use the largest of the three fundamental frequencies since it is stan-

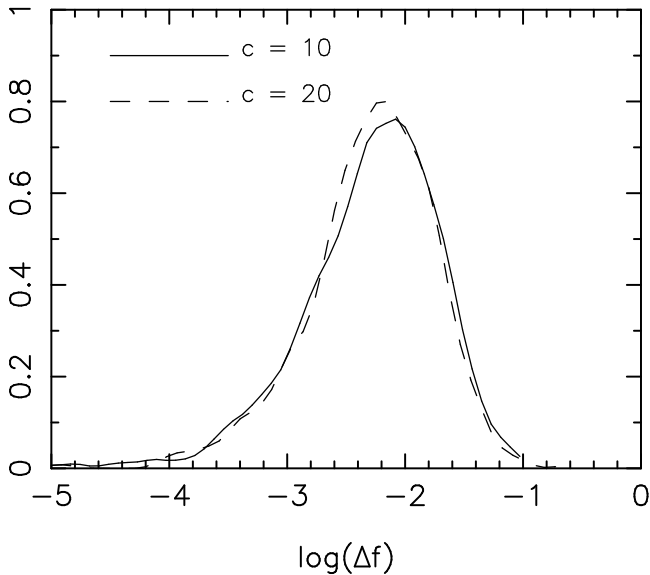


Figure 1. Distributions of frequency drift parameter $\log(\Delta f)$ for 1000 orbits in two different spherical NFW halos. Despite the difference in concentration $c = 10$ and $c = 20$ the distributions are almost identical having a mean of $\log(\Delta f) = -2.29$ and a standard deviation $\sigma \simeq 0.56$, with a significant skewness toward small values of $\log(\Delta f)$.

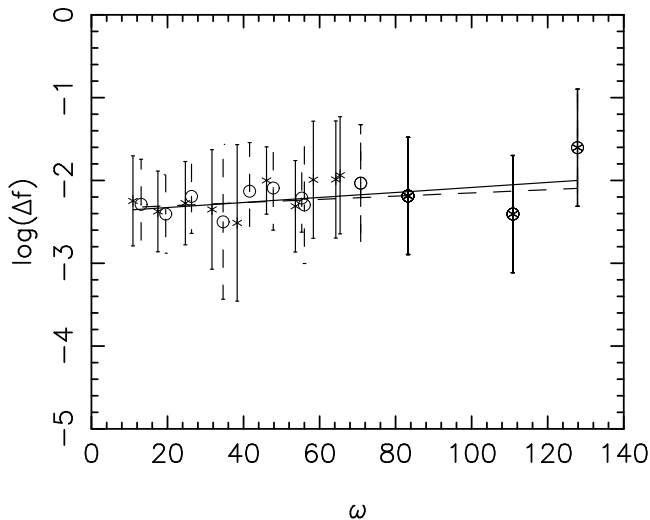


Figure 2. $\log(\Delta f)$ versus ω (in units of Gyr^{-1}) for orbits with $n_p > 20$ in the two spherical NFW halos. Stars are for the halo with $c = 10$ and the open circles are for the halo with $c = 20$. The 1000 particles are binned in ω so that each bin contains the same number of particles. The vertical error bars represent the standard deviation in each bin. The straight lines are fits to the data, the slopes of both lines are consistent with zero.

accurately. Particles are binned in equal intervals in ω and the error bars represent the standard deviation in each bin. The straight-lines are best fits to the data-points. The slopes of the correlation for the $c = 10$ halo (solid line) and for the $c = 20$ halo (dot-dashed line) are both consistent with zero, indicating that $\log(\Delta f)$ is largely independent of ω (and hence of n_p). Henceforth we only use orbits which execute more than 20 orbital periods in the 50 Gyr over which they are integrated. The excluded orbits lie predominantly at large radii and are not significantly influenced by the changes in the inner halo that are investigated here. This rejection criterion affects about 25% of the orbits in the triaxial dark matter halos that we consider later.

The effect of central concentration on the accuracy of frequency estimation is of particular concern during *phase b*, when the potential is deepened due to the growth of a baryonic component. In this phase, frequencies of those orbits which are strongly influenced by the deepened potential are increased. Consequently some orbits execute many more orbital periods during *phase b* than they do in *phase a* or *phase c*. However we have fixed the orbital sampling time period (*not timestep*) to 1 Myr in all phases. In principle coarse time sampling should not be a concern since the long integration time can still ensure a proper coverage of the phase-space torus. To ensure that the sampling frequency per orbital period does not significantly alter the frequency estimation we re-simulated one model (SA1) in *phase b* and stored the orbits 5 times more often (i.e. at time intervals of 0.2 Myr). We compared the frequencies of orbits computed for the low (ω_L) and high (ω_H) time-sampling runs. Figure 3 (*left*) shows that there is a strong correspondence between frequencies obtained with the two different samplings. We also found (Fig. 3 *middle*) that the frequency drift parameter $\log(\Delta f)$ obtained from the two runs are highly correlated although there is some increase in scatter for orbits with values of $\log(\Delta f) > -2$. Since the scattered points lie roughly uniformly above and below the 1:1 correlation line, there is no evidence that the higher sampling rate gives more accurate frequencies. The right panel shows that the overall distribution of $\log(\Delta f)$ is identical for the two runs. We find that 95% of the particles showed a frequency difference $< 0.1\%$ between the two different sampling rates. From these tests we conclude that our choice of sampling rate in the *phase b* is unlikely to significantly affect the frequency measurements of the majority of orbits. As we will show later, this model (*phase b* of SA1) has the largest fraction of chaotic orbits, and frequency measurement is extremely unreliable for such orbits. It is likely that the orbits with large differences between ω_L and ω_H are mostly chaotic orbits. We therefore adopt the lower orbit sampling frequency for all the analysis that follows.

standard practice to use the change in this quantity over time to measure frequency drift (Laskar 1990). For situations where a large fraction of orbit are resonant, it may be more appropriate to use the smallest of the three frequencies.

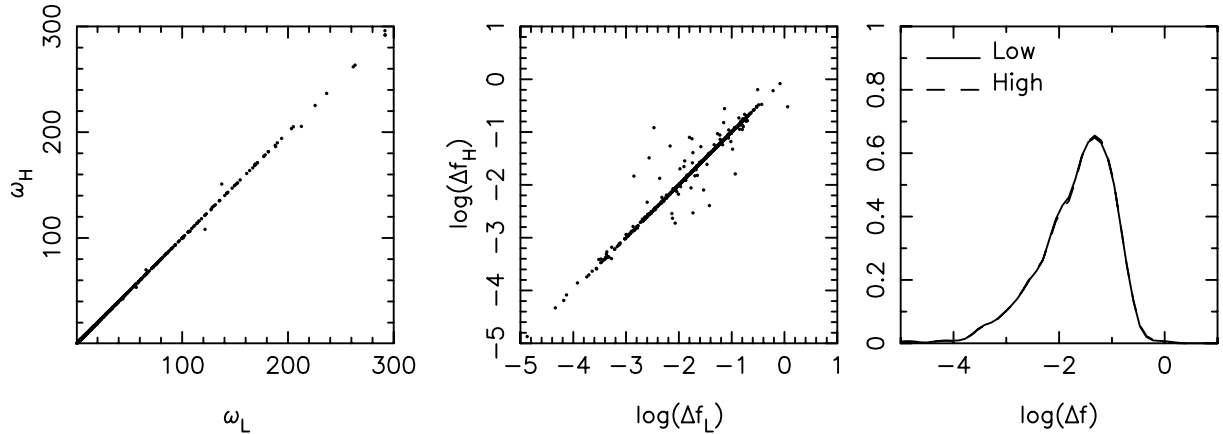


Figure 3. *left:* comparison of frequencies computed from the low and high time-sampling runs ω_H versus ω_L respectively; *middle:* comparison of diffusion parameter $\log(\Delta f)$ measured in low and high sampling runs; *right:* histograms of diffusion parameter $\log(\Delta f)$.

3.2 Orbit classification

Carpintero & Aguilar (1998, hereafter CA98) showed that once a frequency spectrum of an orbit is decomposed into its fundamental frequencies, the relationships between the values of the frequencies ($\omega_x, \omega_y, \omega_z$) can be used to classify the orbits in a triaxial potential into the major orbit families as boxes, long (x) axis tubes and short (z) axis tubes. (CA98 point out that it is difficult to distinguish between the inner long-axis tubes and outer long-axis tubes from their frequencies alone. Therefore we do not attempt to distinguish between these two families with our automatic classification scheme.) In addition to classifying orbits into these three broad categories, they showed that if one or more of the fundamental frequencies is an integer linear combination of the other frequencies, the orbit can be shown to be resonant (either a periodic orbit or an open resonance). We followed the scheme outlined by CA98 to develop our own algorithm to classify orbits as boxes, long-axis tubes (abbreviated as L-tubes), short-axis tubes (abbreviated as S-tubes) and to also identify orbits that are associated with low-order resonances. We do not describe the classification scheme here since it is essentially identical to that described by CA98, the main difference lies in that we use NAFF to obtain the fundamental frequencies of orbits in the N -body model, whereas they used a method based on that of Binney & Spergel (1984). We tested our automated classification by visually classifying 60 orbits that were randomly selected from the different models. We then ran our automated orbit classifier on this sample, and compared our visual classification with that resulting from the automated classifier. The two methods agreed for 58/60 orbits (a 96% accuracy rate). Assuming that the visual classification is perfectly accurate, one of the misclassified orbits was a resonant open boxlet (2:3 fish) orbit in the $x - y$ plane which was misclassified as a z -tube. The second was a z -tube with 3 very similar fundamental frequencies which was classified as an x -tube. Hereafter we assume that our automated classification is accurate

96% of the time and therefore any orbit fractions quoted have an error of $\pm 4\%$.

3.3 Quantifying orbital shapes

In any self-consistent potential the distribution of shapes of the majority of the orbits match the overall shape of the density profile. The elongation along the major axis is provided either by box orbits or by inner L-tubes. The ratios of the fundamental frequencies of orbits can be used to characterise their overall shape. Consider a triaxial potential in which the semi-major axis (along the x -axis) has a length a_x , the semi-intermediate axis has length a_y , and the semi-minor axis has a length a_z . The fact that $a_x > a_y > a_z$ implies that the oscillation frequencies along these axes are $|\omega_x| < |\omega_y| < |\omega_z|$ for any (non resonant) orbit with the same over-all shape as the density distribution (we consider only the amplitudes of the frequencies since their signs only signify the sense of oscillation). We can use this property to define an average ‘‘orbit shape parameter’’ (χ_s) for any orbit. For an orbit whose overall shape matches the shape of the potential,

$$\begin{aligned}
 & |\omega_z| > |\omega_y| > |\omega_x| \\
 \Rightarrow & \frac{|\omega_y|}{|\omega_z|} > \frac{|\omega_x|}{|\omega_z|} \\
 \chi_s \equiv & \frac{|\omega_y|}{|\omega_z|} - \frac{|\omega_x|}{|\omega_z|} > 0.
 \end{aligned} \tag{3}$$

The orbit shape parameter χ_s is positive for orbits with elongation along the figure. The larger the value of χ_s , the greater the degree of elongation along the major axis. Very close to the centre of the potential it is possible for orbits to have greater extent along the y axis than along the x axis as is sometimes the case with outer L-tubes. For such orbits χ_s is slightly negative. An orbit for which all frequencies are almost equal would enclose a volume that is almost

spherical. For such an orbit, $\chi_s \sim 0$ (which we refer to as “round”). (Note that orbits which are close to axisymmetric about the short (z) axis (i.e. the short axis tubes) also have $\chi_s \sim 0$ because $\omega_x \sim \omega_y$ regardless of the value of ω_z . Our definition of shape parameter does not permit us to distinguish between truly round orbits for which $\omega_x \sim \omega_y \sim \omega_z$ and S-tubes, but both contribute to a more spherical potential.)

4 RESULTS

For every model in Table 1 the three fundamental frequencies $\omega_x, \omega_y, \omega_z$ of each of the orbits in a selected subsample were computed separately in each of the three phases. For each orbit the largest of the three fundamental frequencies is assumed to represent the dominant frequency of motion. The absolute value of this quantity is referred to as the largest fundamental frequency: we use $\omega_a, \omega_b, \omega_c$ to refer to the largest fundamental frequencies of an orbit in each of the three phases a, b, c . In addition to computing the fundamental frequencies over the entire 50 Gyr interval, we split the interval into two equal halves and computed the frequencies in each to compute the frequency drift parameter $\log(\Delta f)$ defined in §3. All orbits with $\log(\Delta f) < -1.0$ are identified as regular and the rest are identified as chaotic. For each orbit we also compute the total energy (E), the absolute value of the total specific angular momentum ($|j_{\text{tot}}|$), the number of orbital periods (n_p), and the pericenter and apocenter distance from the centre of the potential ($r_{\text{peri}}, r_{\text{apo}}$).

In this section we consider results of 4 simulations, SA1, P_IA3, P_fB2, and P_IB3. The baryonic components in these simulations can be thought of as representing a disk galaxy, two elliptical galaxies and a massive compact bulge, respectively. As we shall see, halos A and B have very different initial orbital properties even though they are grossly similar (compare Figures 3a and 3g of D08).

4.1 Distributions of orbital frequencies

The frequency distribution of randomly selected orbits in a triaxial halo can be used to characterise the orbital structure of phase space. It is useful to begin by discussing our expectations for how orbital frequencies change in response to growth of a central baryonic component. The potential is significantly deeper in *phase b* compared to *phase a*, consequently the most tightly bound orbits in the initial potential increase their frequency. In contrast orbits which largely lie outside the central mass concentration do not experience much deformation or much change in their frequencies. The higher the initial frequency the greater will be the frequency increase. Hence we expect a faster-than-linear increase in frequency in *phase b* relative to the frequency in *phase a*.

When the baryonic component is evaporated, the halo expands once more and D08 showed that the halos regain their triaxiality

in models SA1, P_IA3 and P_fB2 but are irreversibly deformed in model P_IB3. One way to investigate the cause of the difference in these behaviours is to look for correlations between largest fundamental frequencies of each orbit in each of the three phases. In Figure 4 we plot correlations between the frequencies ω_a, ω_b and ω_c . The panels on the left show that ω_b increases faster-than-linearly with ω_a , as expected. The left panels also shows that the growth of the baryonic component changes the frequency ω_b in a regular (i.e. monotonic) way in three of the four models (SA1, P_IA3 and P_fB2), but in P_IB3 there is a great deal of scatter.

The right hand panels show that ω_c is quite tightly correlated with ω_a for simulation SA1 indicating that most orbits recover their original frequencies following the evaporation of the baryonic disk. The deviation from the dashed line and the scatter is only slightly larger in simulations P_IA3 and P_fB2. The strong correlation between ω_c and ω_a in these models supports the argument by D08 that the growth of the baryonic component resulted in regular rather than chaotic evolution of the phase space. In all three models only a small fraction of points deviate from the dashed line for the highest frequencies. Those that deviate lie systematically below the line indicating a slight decrease in frequency. This corresponds to an increase in total particle energy implying that there has been a slight expansion in the DM distribution following the evaporation of the baryonic component.

On the other hand, simulation P_IB3 shows significantly more scatter in both ω_b and ω_c . Contrary to our expectation that in response to the deepening of the central potential ω_b will increase, we see that it is sometimes decreased. This is evidence of an orbit being *scattered* in frequency rather than experiencing a regular adiabatic change. Run P_IB3 has the most compact baryonic component. Clearly, a hard point mass can produce significant chaotic scattering.

What fraction of orbits experience a large fractional change in frequency of an orbit from *phase a* to *phase b*, and from *phase a* to *phase c*? To investigate this we define:

$$\Delta\omega_{ab} = |(\omega_a - \omega_b)/\omega_a| \quad (4)$$

$$\Delta\omega_{ac} = |(\omega_a - \omega_c)/\omega_a|. \quad (5)$$

The first quantity is a measure of the change in frequency distribution of orbits induced by the presence of the baryonic component, while the latter quantity measures the irreversibility of the evolution. In Figure 5 we plot kernel density histograms of distribution of the frequency change $\Delta\omega_{ab}$ (left panel) and $\Delta\omega_{ac}$ (right panel) for orbits in all four models.

The distribution of $\Delta\omega_{ab}$ is much wider for models P_IA3 and P_IB3 than for the other two models. In these two models the size of the baryonic component is ≤ 1 kpc and results in a broad distribution of $\Delta\omega_{ab}$, indicating that orbits over a wide range of frequencies experience significant frequency change.

The right panels show that only a small number of orbits in models SA1, P_IA3 and P_fB2 experience an irreversible frequency change $\Delta\omega_{ac} > 20\%$, with the majority of particles experiencing

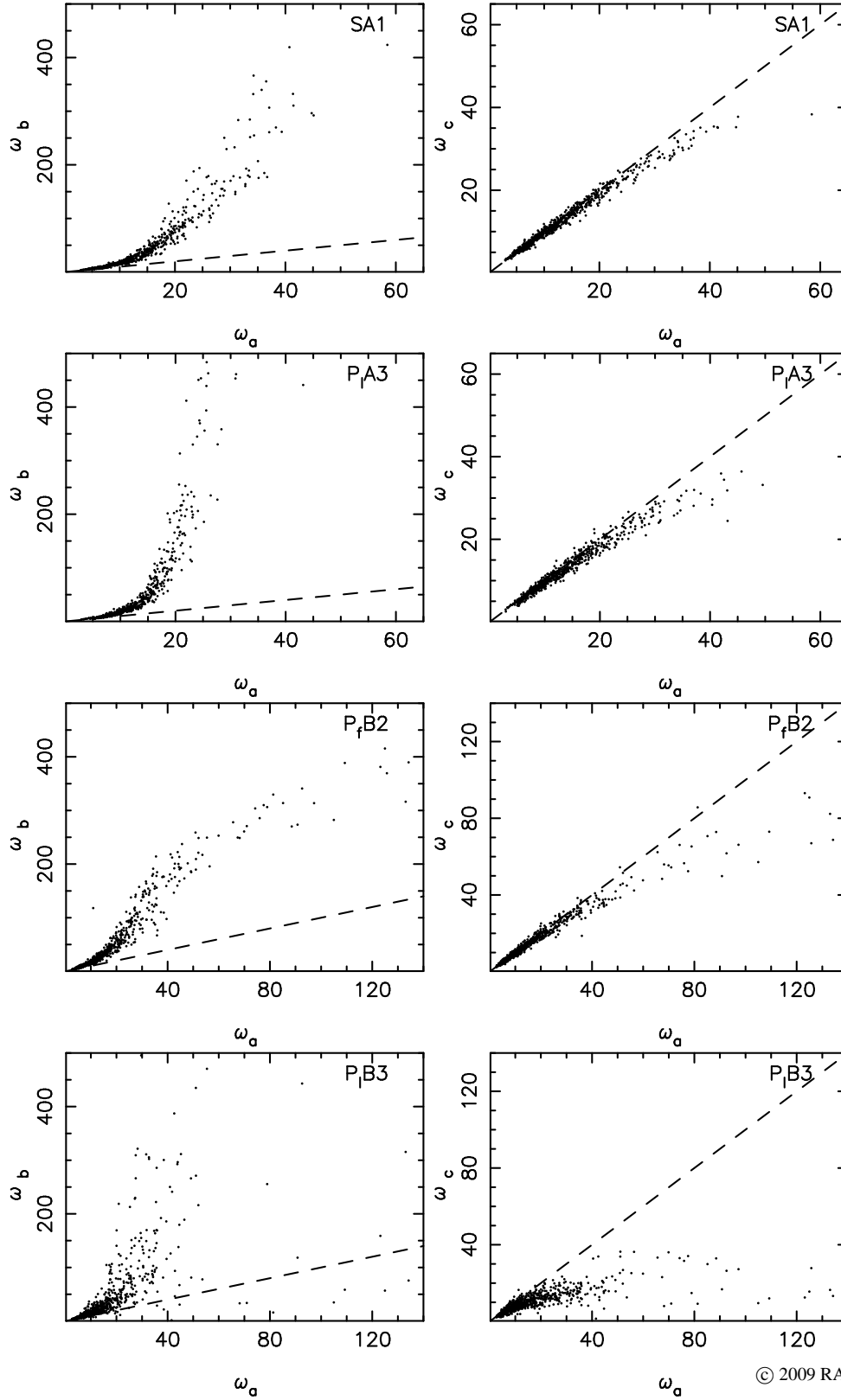


Figure 4. For each of four models: *left panels* show ω_b versus ω_a and *right panels* show ω_c versus ω_a (frequencies in Gyr^{-1}). Dashed lines in each panel show the 1:1 correlation between each pair of frequencies.

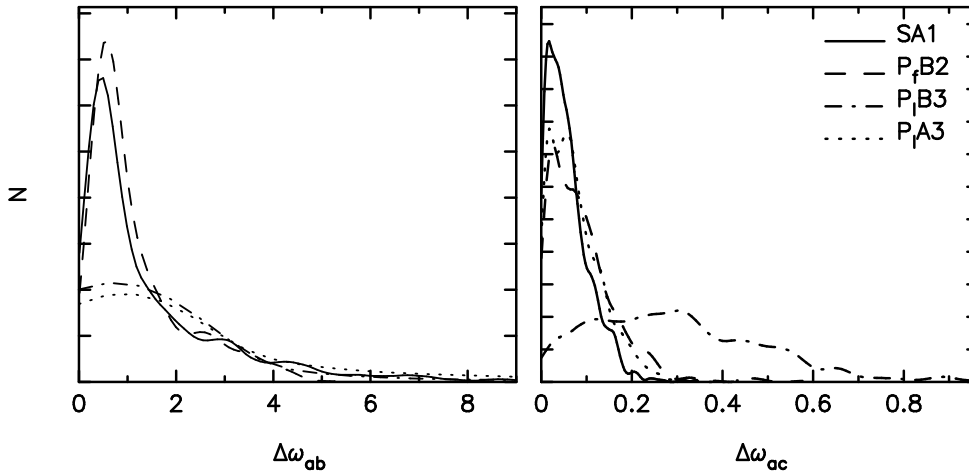


Figure 5. Kernel density distributions of $\Delta\omega_{ab}$ (left panel) and of $\Delta\omega_{ac}$ (right panel) for particles in the halos SA1, P_fB2, P_lB3 and P_lA3 as indicated by line legends. The vertical scale on each histogram is arbitrary with each curve normalised to unit integral.

less than 10%. In contrast in model P_lB3, the distribution of $\Delta\omega_{ac}$ is much broader: a significant fraction of particles have experienced a large (20-50%) permanent change in their frequencies, reflecting the fact that this model suffers the most irreversibility.

Are there specific orbital characteristics that contribute to a large permanent frequency change, $\Delta\omega_{ac}$, between the two triaxial phases? We address this by determining how this quantity relates to other orbital properties. In Figure 6 we plot $\Delta\omega_{ac}$ versus ω_a (left panels) and versus ω_b (right panels). In models SA1, P_lA3 and P_fB2 there is no evidence of a dependence of frequency change on ω_b and only a slight increase in $\Delta\omega_{ac}$ at the highest values of ω_a . In model P_lB3, on the other hand, we see a strong correlation between $\Delta\omega_{ac}$ and orbital frequency ω_a indicating that the orbits with the highest frequencies experience the largest frequency change. This is evidence that scattering by the hard central point mass is greatest for particles that are most tightly bound and therefore closest to the central potential in model P_lB3 and confirms previous expectations (Gerhard & Binney 1985; Merritt & Valluri 1996). The absence of an appreciable correlation with ω_b is the consequence of scattering of orbits in *phase b*. Another consequence of the scattering is the tangential bias which develops in the inner ~ 5 kpc of this model (see Figure 5 of D08). This was the only model in which growth of a baryonic component led to tangential bias, rather than the radial bias that is expected to arise from baryonic compression.

In Figure 7 we plot $\Delta\omega_{ac}$ versus r_{peri} (left panels) and versus $|j_{\text{tot}}|$ (the total specific angular momentum of an orbit averaged over its entire orbit in *phase a*) (right panels) for each orbit in model P_lB3 only. (We do not show plots for models SA1, P_lA3 and P_fB2, because they show no correlation between $\Delta\omega_{ac}$ and either $|j_{\text{tot}}|$ or r_{peri} .) The left panel of Figure 7 shows that orbits which pass closest to the central point mass experience the most significant scattering, as is to be expected since the central particle is very

compact. This indicates that the primary cause for the irreversible change in shape experienced by model P_lB3 is the result of strong scattering by the point mass of orbits with small pericenter distance. The absence of a correlation with $|j_{\text{tot}}|$ indicates that scattering is independent of the angular momentum of the orbit. (In the next section we show that this model, being initially prolate, has very few box orbits and is dominated by L-tubes which a large angular momentum about the long axis.) Since the point mass is live, it is free to move about and does so in response to gravitational interactions with DM particles. The central point mass wanders about the centre, with a maximum radial excursion of ~ 0.1 kpc. This results in some effect even on the centro-phobic inner L-tubes. Particles with $r_{\text{peri}} < 0.1$ kpc experience greater change in $\Delta\omega_{ac}$ than particles outside this radius, but large $\Delta\omega_{ac}$ is seen well outside this radius indicating that scattering is not due to motion of the black hole alone, but due to the strong deflection of orbits by the deeper and more spherical central potential.

4.2 Changes in Orbital Classification

As we discussed in § 3.2, relationships between the fundamental frequencies of a regular orbit can be used to classify it as a box orbit, a L-tube or a S-tube orbit. Quantifying the orbital composition of the two different halos A and B and how their compositions change in response to the growth of a baryonic component yield further insight into the factors that lead to halo shape change. Orbits were first classified as regular or chaotic based on their drift parameter $\log(\Delta f)$ as described in § 3.1. Regular orbits were then classified into each of three orbital families using the classification scheme outlined in § 3.2. The results of this orbit classification for each model, in each of the three phases, are given in Table 2.

The most striking difference between the initial (*phase a*) tri-

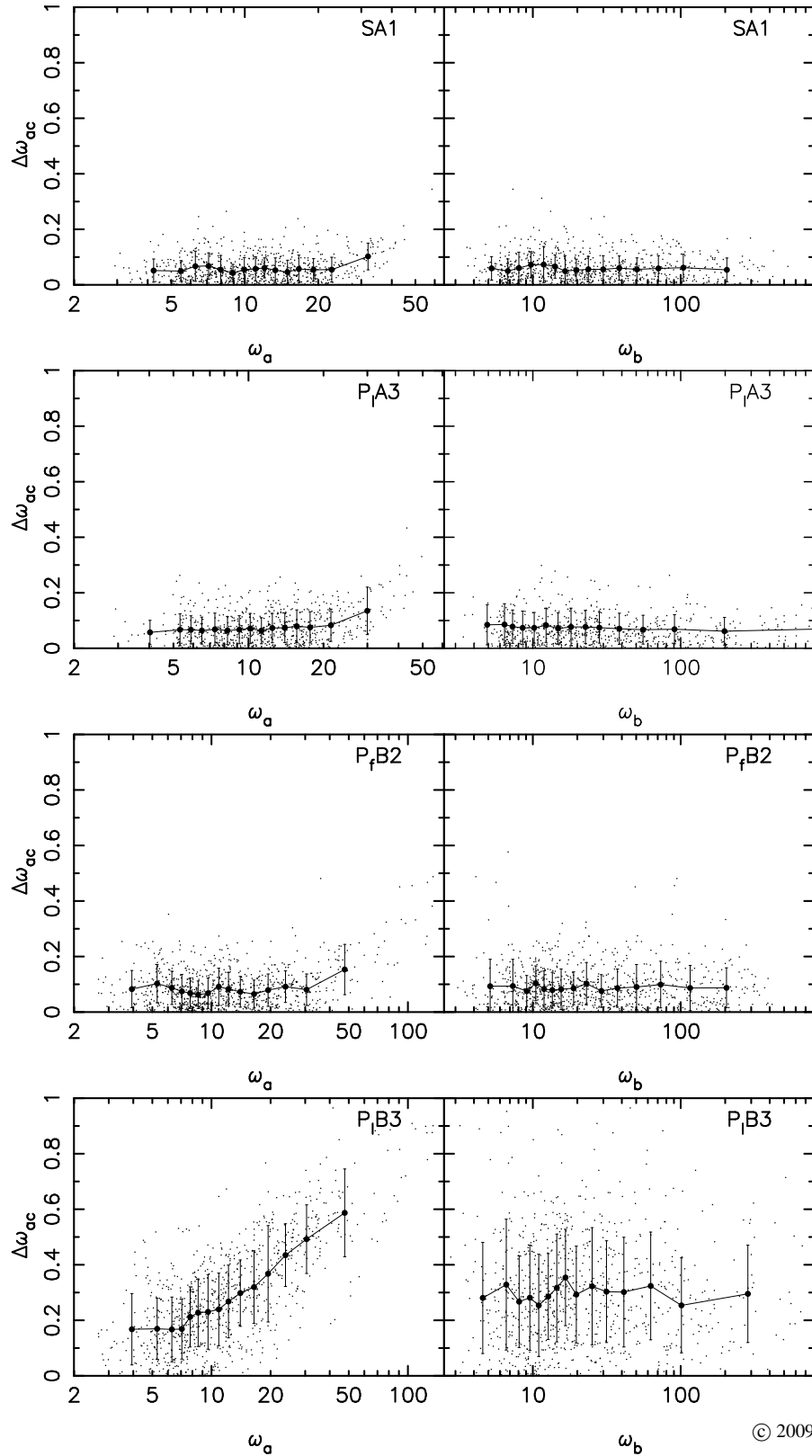


Figure 6. For each of four models small dots show $\Delta\omega_{ac}$ versus ω_a (left) and versus ω_b (right) for all particles analysed. Large solid dots with error bars show mean and standard deviation of particles in 15 bins in frequency. $\Delta\omega_{ac}$ is independent of ω_b and only shows a slight increase with ω_a in the highest frequency bin for models SA1, P_fB2 and P_lA3 . In model P_lB3 instead $\Delta\omega_{ac}$ increases significantly with ω_a and is significantly larger than in any of the other models.

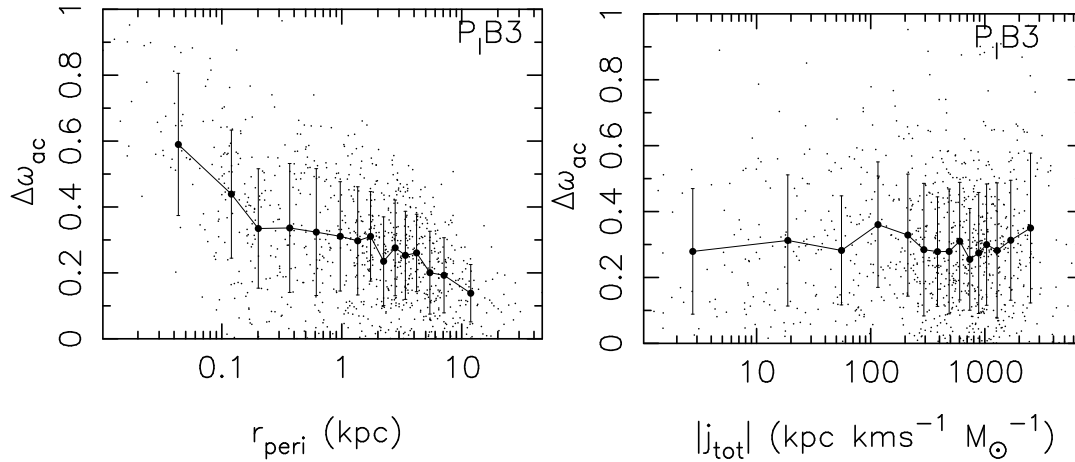


Figure 7. For model P₁B3 left: $\Delta\omega_{ac}$ versus r_{peri} ; right: $\Delta\omega_{ac}$ versus $|j_{\text{tot}}|$.

Table 2. Orbit composition of the models. The numbers represent the fraction of orbits in each family.

| Orbit Type | Run SA1 | | | Run P ₁ A3 | | | Run P _f B2 | | | Run P ₁ B3 | | |
|----------------|---------|---------|---------|-----------------------|---------|---------|-----------------------|---------|---------|-----------------------|---------|---------|
| | Phase a | Phase b | Phase c | Phase a | Phase b | Phase c | Phase a | Phase b | Phase c | Phase a | Phase b | Phase c |
| Boxes | 0.86 | 0.43 | 0.83 | 0.84 | 0.16 | 0.76 | 0.15 | 0.09 | 0.29 | 0.15 | 0.03 | 0.21 |
| L-Tubes | 0.11 | 0.09 | 0.12 | 0.12 | 0.43 | 0.15 | 0.78 | 0.75 | 0.54 | 0.78 | 0.78 | 0.59 |
| S-Tubes | 0.02 | 0.27 | 0.03 | 0.02 | 0.32 | 0.06 | 0.07 | 0.09 | 0.16 | 0.07 | 0.11 | 0.14 |
| Chaotic | 0.01 | 0.21 | 0.02 | 0.02 | 0.09 | 0.04 | 0.00 | 0.07 | 0.01 | 0.00 | 0.08 | 0.06 |

axial models is that halo A (of models SA1(disk) and P₁A3 (elliptical)) is dominated by box orbits (84-86%) while halo B (of models P_fB2 (elliptical) and P₁B3 (compact bulge)) is dominated by L-tubes (78%). (The difference between model SA1 and P₁A3 in *phase a* is purely a consequence of the selection of different subsets of orbits in the two halos.) None of the initial models has a significant fraction of S-tubes or of chaotic orbits.

The very different orbit compositions of halos A and B in *phase a* results in rather different evolutions of their orbital populations in response to the growth of a central baryonic component. In model SA1, the growth of the disk results in a significant decrease in the box orbit fraction (from 86% to 43%) with boxes being converted to either S-tubes or becoming chaotic. The decrease in the fraction of box orbits is generally assumed to be the consequence of chaotic scattering but we see again that the evolution in this halo is highly reversible since the box orbit fraction in *phase c* is 83%, consistent with the original population (within the margin of error of our classification scheme). In model P₁A3, the slightly more compact spherical baryonic component decreases the fraction of box orbits even more dramatically (from 84% down to 16%), pointing to the vulnerability of box orbits to perturbation by a cen-

tral component. Model P₁A3 shows slightly less reversibility than model SA1, with the fraction of box orbits in *phase c* dropping to 76%. It appears that in P₁A3, the more compact central point mass does in fact make it harder for box orbits to survive, and they are replaced roughly equally by the two stable tube families.

In contrast with halo A, halo B is initially dominated by L-tubes. Interestingly this family dominates in all three phases. The box orbit fraction decreases in *phase b* (especially in model P₁B3) and the fractions of L-tubes and chaotic orbits increase slightly. The more extended point mass in P_fB2 causes a larger fraction of L-tubes to transform to orbits of another type than does the harder point mass in P₁B3, despite the fact that there is much greater scattering in the latter model. While it is difficult to determine exactly why this is the case, the most likely cause is the more extended nature of the point mass in P_fB2 (where R_d is 3 kpc) than in P₁B3 (where R_d is 1 kpc.)

A significant fraction (21%) of the orbits in *phase b* of model SA1 are classified as chaotic (orbits with drift rate $\log(\Delta f) > -1.0$), in comparison with 9%, 7% and 8% in models P₁A3, P_fB2 and P₁B3 respectively. The presence of such a large fraction of chaotic orbits in *phase b* of model SA1 is puzzling. To address con-

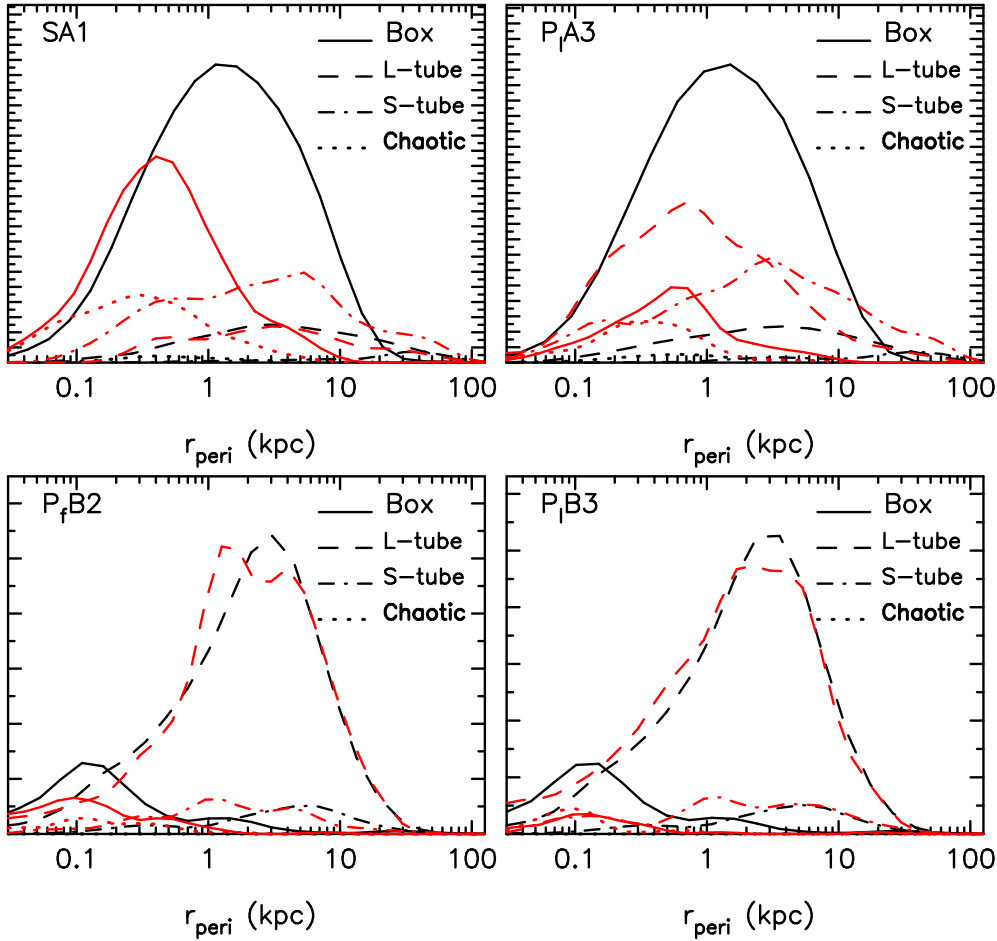


Figure 8. Distributions of r_{peri} for different orbit types. Distributions of each of the four different orbital types as indicated by the line-legends. Distribution in *phase a* is given by black curves and distribution in *phase b* is shown by red curves. The integral under each curve is proportional to the number of orbits of that orbital type.

cerns about classification error that could arise from errors in the accuracy of our frequency computation, we showed, in Figure 3, that changing the frequency at which orbits were sampled by a factor of five did not result in any change in the overall distribution of $\log(\Delta f)$, and hence should not affect our classification of orbits as regular or chaotic. Another puzzling fact is that, although model SA1 in *phase b* has such a significant fraction of chaotic orbits, the orbit fractions essentially revert almost exactly to their original ratios once the disk is evaporated in *phase c*. Hence, the large fraction of chaotic orbits in *phase b* do not appear to cause much chaotic mixing. We will return to a more complete investigation of this issue in § 4.4.

In Figure 8 we investigate how orbits of different types (boxes, L-tubes, S-tubes, chaotic) are distributed with r_{peri} , and how this distribution changes from *phase a* (black curves) to *phase b* (red

curves). The plot shows that in both phases, halo A models are dominated by box orbits. We see that in the halo A models, the distributions with pericenter are quite similar for all orbit families in both phases. Halo B models are instead dominated by L-tubes in both phases. Rather striking is how little the fraction of L-tubes in the halo B models changes, despite the fact that all the halos are significantly more spherical in *phase b* than in *phase a*. We saw in Figure 5 that a significant fraction of orbits experience strong scattering that manifests as a change in their orbital frequencies, and in Figure 7 we noted that the orbits with the smallest pericenter radii experience the largest change in frequency. In halo B the box orbits have significantly smaller r_{peri} in both phases and in model P_fB3, there is a significant reduction in the box orbit fraction, confirming that the central point mass is responsible for the destruction of these box orbit. However it seems unlikely that the destruction of

such a small fraction (15%) of box orbits is entirely responsible for driving the evolution of halo shape. The distribution of L-tubes in Figure 8 is skewed with a tail at small r_{peri} suggesting that a significant number of these orbits too have small pericenter radii. We believe that these L-tubes are also experiencing scattering, but since they have high angular momentum about the x -axis they are merely scattered on to another L-tube orbit rather than onto an orbit of a different type. It is clear (from Fig. 8) that in the prolate models (Halo B) the majority of the orbits are L-tubes with large pericenter radii ($\langle r_{\text{peri}} \rangle \sim 3$ kpc) and these remain L-tubes in *phase b*. How then do these prolate models evolve to more spherical models while retaining their dominant orbit populations? To address this question we will now investigate the distribution of orbital shapes in each model at each phase of the evolution.

4.3 Changes in orbital shape

A parameter to quantify the shape of an orbit χ_s was defined in Equation 3 of § 3.3. Recall that this quantity is positive when the orbit is elongated along the major axis of the triaxial figure, is negative when elongated along the intermediate axis, and almost zero when the orbit is “round” or roughly axisymmetric about the minor axis. In Figure 9 we show the shape distributions for the orbits in the four models. For each model we show kernel density histograms for models in *phase a* (solid curves), *phase b* (dot-dashed curve), and *phase c* (dashed curves). In each plot the curves are normalized such that the integral under each curve is unity. We define orbits to be elongated if $\chi_s \gtrsim 0.25$, and to be “round” if $|\chi_s| \leq 0.1$.

In *phase a* (solid curves) of the halo A models (top panels SA1, P_lA3), the distribution of orbital shapes is bimodal with a large peak at $\chi_s \sim 0.35$, arising from elongated orbits and a very small peak at $\chi_s \sim 0$ due to round orbits. In this phase, the distribution of χ_s is also bimodal for halo B models (bottom panels P_fB2, P_lB3), but about one third of all orbits contribute to the peak at $|\chi_s| \leq 0.1$, i.e. there are significant fractions of round orbits. In both halo A and B however, the peak of χ_s is at about 0.35, despite the fact that the underlying orbital distributions are quite different. Recall that in *phase a* the halo A models are dominated by box orbits while the halo B models are dominated by L-tubes. This illustrates the fact that rather different orbital compositions with similar elongations can result in similarly shaped density distributions.

The dot-dashed curves in all the panels show the distribution of orbital shapes in *phase b*. In all four models there is a dramatic increase in the peak at $|\chi_s| \leq 0.1$, pointing to a large increase in the fraction of round orbits at the expense of the elongated orbits. In the halo B models the elongated orbits are significantly diminished indicating that the elongated L-tubes in *phase a* are easily deformed to round L-tubes in *phase b* (most likely squat inner long axis tubes). However, in model SA1 there are a large fraction of orbits with intermediate values of elongation $\chi_s \simeq 0.2$.

In *phase c* (dashed curves) all models show the dominant peak shifts back to high elongation values, but slightly lower values

($\chi_s \sim 0.3$) than in *phase a*. The downward shift in the peak is largest in model P_lB3, which as we saw before, exhibits the greatest irreversibility in shape. The scattering of a large fraction of the orbits by the hard central potential in model P_lB3 seen in Figures 6 and 7 is the major factor hindering reversibility of the potential. The smallest shift is for model SA1, which exhibited the greatest reversibility.

We can also investigate how the shapes of orbits vary with pericentric radius. We expect that orbits closer to the central potential should become rounder ($\chi_s \rightarrow 0$) than orbits further out. We see that this expectation is borne out in Figure 10 where we plot orbital shape parameter χ_s versus r_{peri} in both *phase a* (left hand plots) and *phase b* (right hand plots). In each plot the dots show values for individual orbits. The solid curves show means of the distribution of points in 15 bins in r_{peri} . Curves are only plotted if there are more than 30 particles in a particular orbital family. We used a kernel regression algorithm to smooth the curves. For models SA1 and P_lA3 the figure confirms that elongated orbits in the initial halo A were box orbits (black dots and curves) and L-tubes (blue dots and curves). The S-tubes (green dots and curves) are primarily responsible for the “round” population at $\chi_s \sim 0$. In *phase b* (right-hand panels) of both SA1 and P_lA3 there is a clear tendency for the elongated orbits (boxes, L-tubes and chaotic) to become rounder at small pericenter distances, but they continue to be somewhat elongated at intermediate to large radii. Chaotic orbits in *phase b* of model SA1 appear to span the full range of pericentric radii and are not confined to small radii. (Note that the density of dots of a given colour is indicative of the number of orbits of a given type but the relative fractions are better judged from Fig. 8.)

For *phase a* in the models P_fB2 and P_lB3 (lower two left panels), boxes and L-tubes are elongated ($\chi_s \geq 0.25$) (except at large $r_{\text{peri}} \geq 8$ kpc where they become rounder). Once again we see a trend for orbit shapes in *phase b* (especially in the box and chaotic orbit families) to become round ($\chi_s \rightarrow 0$) at small pericenter radii.

Thus in all four models it is clear that orbits that are elongated along the major axis of the triaxial potential in *phase a* become preferentially rounder at small pericenter radii in *phase b*. It is this change in orbital shape that plays the most significant role in causing the overall change in the shape of the density in the baryonic phase.³

4.4 Frequency maps and chaotic orbits

We saw in Table 2 that *phase b* of model SA1 (Halo A+disk) has the largest fraction (21%) of chaotic orbits (i.e. orbits with $\log(\Delta f) > -1$). Figure 11 shows kernel density histograms of the chaotic drift parameter $\log(\Delta f)$ for orbits in each of the three phases in model SA1. It is obvious that in *phases a* and *c* there is only a small fraction of chaotic orbits (i.e. orbits with $\log(\Delta f) > -1$), whereas a

³ Due to our chosen definition of shape parameter, S-tubes generally appear “round” regardless of radius, because $\omega_x \sim \omega_y$.

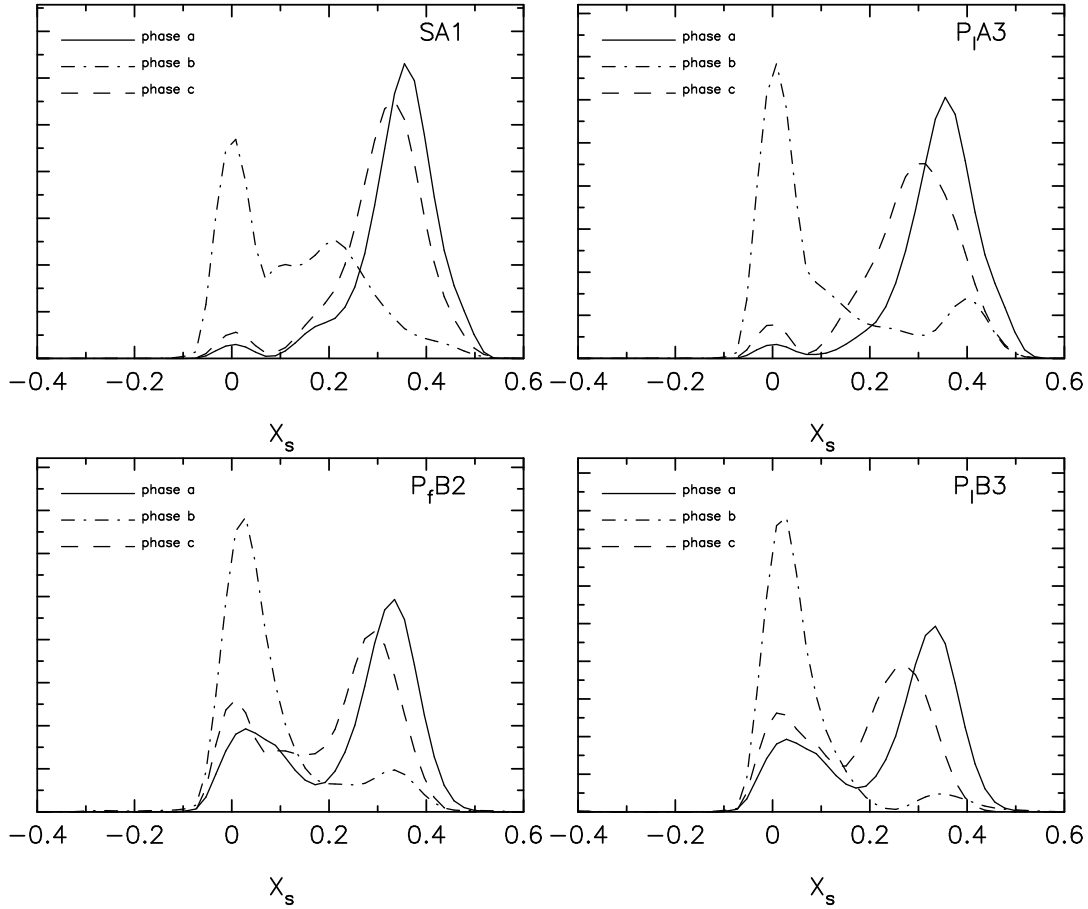


Figure 9. Kernel density histograms of the distribution of orbital shape parameter χ_s for each of the four models: SA1 (*top left*), P₁A3 (*top right*), P_fB2 (*bottom left*) and P₁B3 (*bottom right*). Distributions of χ_s in *phase a* are shown by solid curves, in *phase b* by dot-dashed curves, and in *phase c* by dashed curves. In all models, a large fraction of orbits in *phase b* are “round” ($|\chi_s| \leq 0.1$.)

much more significant fraction of orbits lie to the right of this value in *phase b*. Even the peak of the distribution in *phase b* is quite significantly shifted to higher drift values.

Yet despite having a large fraction of chaotic orbits, SA1 is the model that shows the greatest reversibility in the evolution from *phase a* to *phase b* to *phase c*! This is quite surprising since the presence of a large fraction of chaotic orbits is expected to cause irreversible evolution of orbital properties (Merritt & Valluri 1996). One possible reason for the lack of diffusion of the chaotic orbits is that the timescale for evolution is not long enough. Indeed D08 report that evolving run SA1 with the disk at full mass for an additional 5 Gyr after the growth of the disk is complete, leads to a larger irreversible evolution (see their Figure 3a). Nonetheless, even in that case the irreversible evolution was only marginally larger than when the disk was evaporated right after it grew to full mass.

Moreover the growth time was 5 Gyr which means that the halo was exposed to a massive disk for a cosmologically long time.

A second possible reason for the lack of chaotic diffusion is that most of the chaotic orbits in this phase of the simulation are “sticky”. To understand the relevance of “sticky” chaotic orbits, it is necessary to first discuss the structure of phase space in greater detail. When an integrable potential is perturbed, its phase space structure is altered, resulting in the appearance of resonances. Resonances are regions of phase space where the three fundamental frequencies are not linearly independent of each other, but two or more of them are related to each other via integer linear relations. As the perturbation in the potential increases a larger and larger fraction of the phase space becomes associated with resonances. In a three dimensional potential, orbits that satisfy one resonance condition such as $l\omega_x + m\omega_y + n\omega_z = 0$ are referred to as “thin orbit” resonances since they cover the surface of a two dimensional sur-

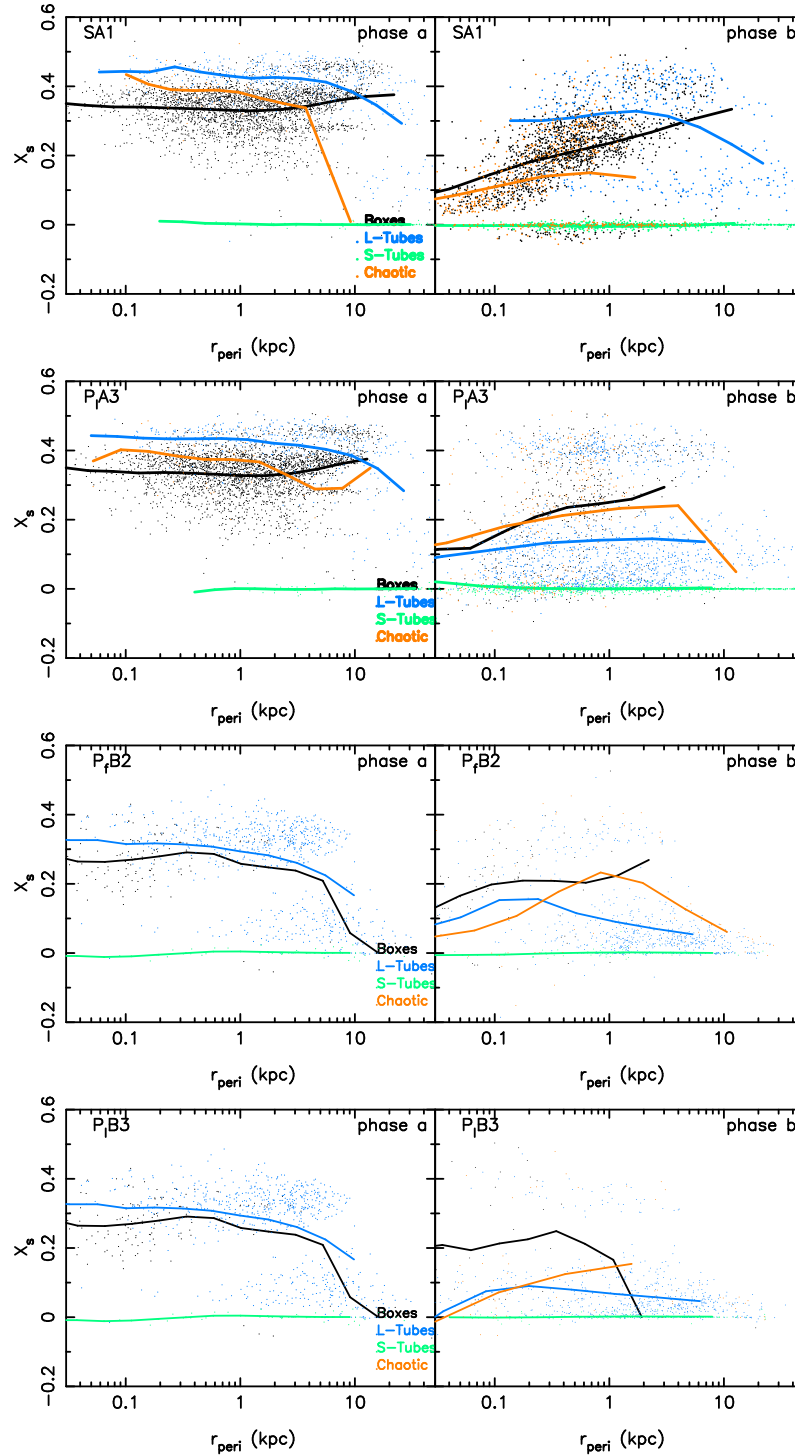


Figure 10. For each of the four models SA1, P_fA3, P_fB2 and P_fB3, the orbital shape parameter χ_s for each orbit is plotted against its pericentric radius r_{peri} as a small dot. The orbits of each of the four major orbital families are colour coded as in the figure legends in the top panel. Left hand panels are for *phase a* and right hand panels are for *phase b*. The solid curves show the mean value of χ_s for all particles of that particular family, in 15 bins in r_{peri} . Curves are not plotted if there are fewer than 30 orbits in a given orbital family.

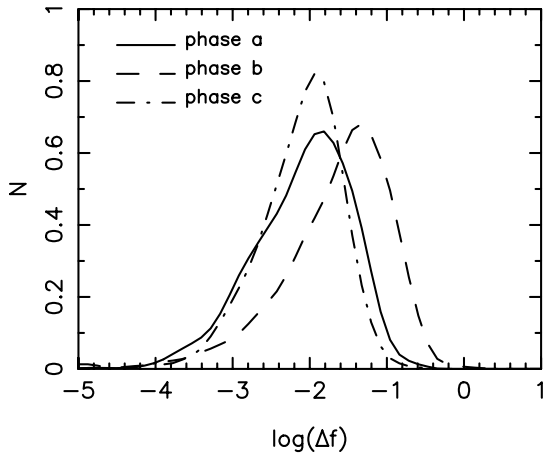


Figure 11. Histograms of frequency drift parameter $\log(\Delta f)$ for the three phases of model SA1 as indicated by the line-legends.

face in phase space (Merritt & Valluri 1999). If two independent resonance conditions between the fundamental frequencies exist, then the orbit is a closed periodic orbit. Orbits that have frequencies close to the resonant orbit frequencies are said to be resonantly trapped. Such orbits tend to have properties similar to that of the parent resonance, but get “thicker” as their frequencies move away from the resonance. At the boundary of the region of phase space occupied by a resonant family is a region called the “separatrix”. The separatrix is the boundary separating orbits with different orbital characteristics. In this case it is the region between orbits that have frequencies that are similar to the resonant orbits and orbits that are not resonant. Chaotic orbits often occur in a “stochastic layer” close to resonances and at the intersections of resonances. In fact one of the primary factors leading to an increase in the fraction of chaotic orbits as a perturbation to an integrable potential is increased is the overlap of resonances (Chirikov 1979). Chaotic orbits that are close to a resonant family are referred to as “resonantly trapped” or “sticky orbits” (Habib et al. 1997) and are often only weakly chaotic. Orbits that are “sticky” behave like the resonant parent orbit for extremely long times and therefore do not diffuse freely over their energy surface or undergo significant chaotic mixing.

Laskar (1990) showed that frequency maps are a powerful way to identify resonances in dynamical systems. Frequency maps are obtained by plotting ratios of the 3 fundamental frequencies for each individual orbit. If a large and representative orbit population is selected, they can provide a map of the phase space structure of the potential including all the resonances. Resonances appear as straight lines on the frequency map. This method of mapping the phase space has the advantage that since it only depends on the ratios of the frequencies and not on the frequencies themselves, it can be used to map phase space for large ensembles of particles without requiring them to be iso-energetic. This is a significant ad-

vantage over mapping schemes like Poincaré surfaces-of-section, when applied to an N -body simulation where particles, by design, are initialised to be smoothly distributed in energy. Thus one can use the method to identify global resonances spanning a large range of orbital energies in N -body simulations.

In Figure 12 we present frequency maps for all four models in *phase a* (left panels) and *phase b* (right panels). For each orbit the ratios of the fundamental frequencies ω_y/ω_z and ω_x/ω_z are plotted against each other. Particles are colour coded by their energy in *phase a*. The energy range in *phase a* was divided into three broad energy bins, with equal numbers of particles per bin. The most tightly bound particles are coloured blue, the least bound particles are coloured red and the intermediate energy range is coloured green. The map for model SA1 has 6000 particles, the map for model P7A3 has 5000 particles and the other two maps have 1000 particles each.

Resonance lines are seen in the clustering of particles in all the maps. The most striking of the frequency maps is that for *phase b* of model SA1 (top right panel). This map has significantly more prominent resonance lines around which many points cluster, than any other map. Three strong resonances and several weak resonances are clearly seen as prominent straight lines of tightly clustered points. The first is a horizontal line at $\omega_y/\omega_z = 1$. This corresponds to the family of orbits associated with the 1:1 closed (planar) orbit that circulates around the x -axis, namely the family of “thin shell” L-tubes. The second resonance is a diagonal line running from the bottom left corner to the top right corner with a slope of unity corresponding to $\omega_y/\omega_z = \omega_x/\omega_z$. This corresponds to the family of z -axis “thin shell” short axis S-tubes which is clearly significantly strengthened in *phase b* compared to *phase a*. In addition to having many more orbits associated with it, it extends over a much wider range in energy (notice the clustering of blue dots which are deep in the potential). The third resonance is the vertical line at $\omega_x/\omega_z = 0.5$ that corresponds to orbits associated with the family of banana (1:2 resonant) orbits.

The dramatic increase in the length and number of particles associated with the diagonal (S-tube) resonance is the result of the growth of the disk, which causes an increase in the mass density in the plane perpendicular to the short (z)-axis. The increase in the strength of the gradient of the potential along the z -axis results in an increase in ω_z , thereby resulting in a decrease in both its ordinate and abscissa on the frequency map. The more tightly bound a particle, the greater the increase in ω_z . This causes the most bound particles (blue points) to move away from their original positions towards the bottom left hand corner of the plot. The least bound particles (red points) are furthest from the center of the potential and these points experience the least displacement - although these points also shift slightly toward the resonance lines. The increase in the total number of points associated with this resonance is the result of “resonant trapping” of halo particles into this 1:1 resonance, by the adiabatic growth of the axisymmetric disk potential which enhances the strength of this resonance. The 1:2 banana resonance

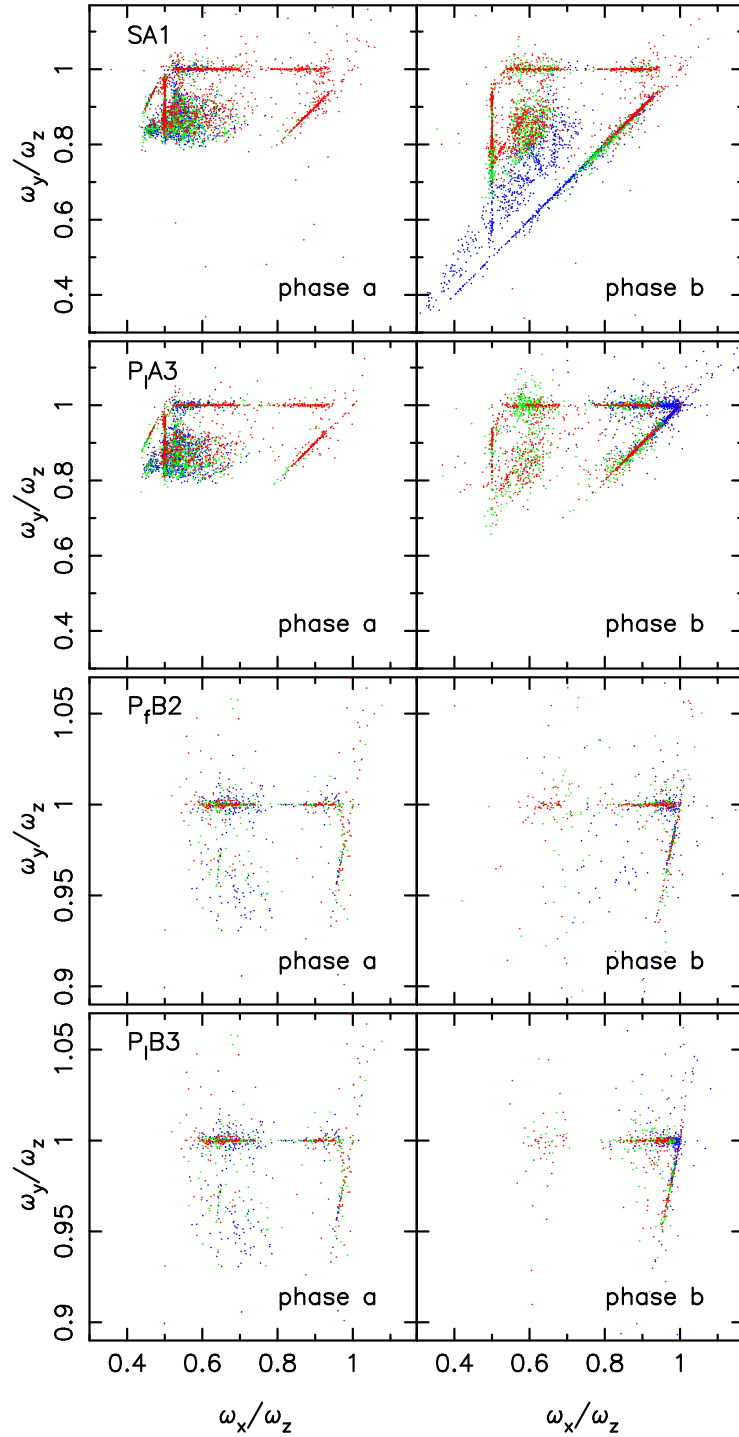


Figure 12. Frequency maps of orbits in *phase a* and *phase b* for the four different models. For each orbit the ratios of the fundamental frequencies ω_y/ω_z are plotted versus ω_x/ω_z , colour coded by their energy in *phase a*. The most tightly bound particles are coloured blue, particles in the intermediate energy range are coloured green, and the least bound particles are coloured red. Model SA1 (halo A + disk) has 6000 particles, model P_lA3 (halo A + elliptical) has 5000 orbits, while the other two models have 1000 particles each.

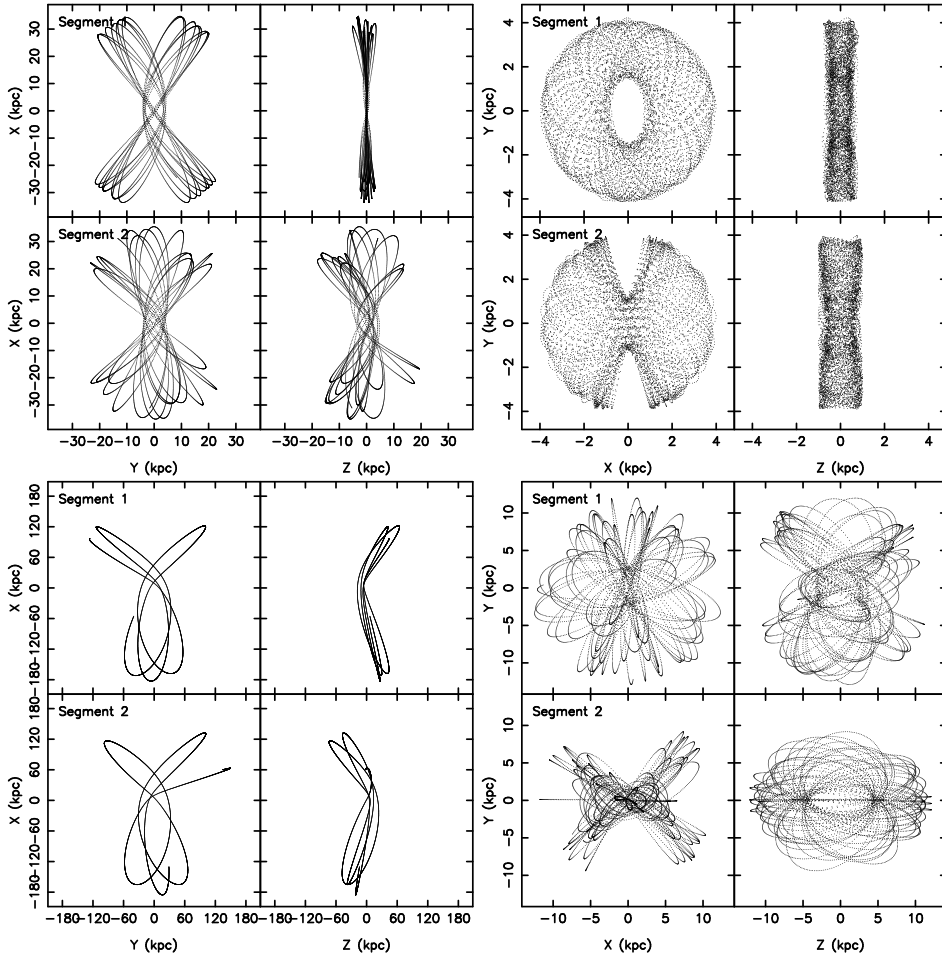


Figure 13. Several chaotic orbits in *phase b* of model SA1. Orbits are plotted in two Cartesian projections over two different time segments of 7.5 Gyr (top two plots in each panel show the first time segment, while bottom panels show the second time segment). See text for details.

is also enhanced by the growth of the disk since this family of orbits, while not axisymmetric, is characterised by large excursions along the x -axis and smaller excursions in the z direction.

The frequency map for model $P_I A3$ shows that a spherical baryonic component produces a rather different phase space structure than that produced by the disk. In particular it is striking that the most tightly bound (blue) points are now clustered at the intersection of the horizontal and diagonal resonances namely around the closed period orbits 1:1:1. This is understandable since the baryonic component is spherical - so no particular frequency direction is preferred and the orbits are all much 'rounder'. The 1:2 banana resonance is also less prominent in this model (largely because the deep central potential destabilises this boxlet family).

The frequency maps for models $P_f B2$ and $P_I B3$ show that most of the orbits in these models are associated with the (1:1)

L-tube family (horizontal lines). A smaller number of orbits is associated with the 1:1 S-tube resonance (diagonal line). We saw previously that the growth of the baryonic components in these halos caused little change in the orbit families. This is confirmed by the frequency maps which are remarkably similar except for a slight increase in the clustering of points along the diagonal (S-tube) resonance. Since Halo B is initially a highly prolate model, it has (as we saw previously) a very small fraction of box (and boxlet) orbits and in particular no banana orbits.

It is quite striking that in *phase a* the frequency maps show significantly less segregation by energy, and only a few resonances. This is because the initial triaxial models were generated out of mergers which tend to distribute orbits smoothly in phase space. The increase in the number of resonances following the growth of a baryonic component is one of the anticipated consequences of

resonant trapping that occurs during the adiabatic change in a potential (e.g. Tremaine & Yu 2000).

To test the conjecture that the majority of chaotic orbits in model SA1 (*phase b*) are resonantly trapped, we compute the number of chaotic orbits that lie close to a major resonance line. We define “closeness” to the resonance by identifying those orbits whose frequency ratios lie $\pm\alpha$ of the resonant frequency ratio. For example we consider an orbit to be close to the (1:1) L-tube resonance (horizontal line in map), if $|\omega_y/\omega_z - 1| \leq \alpha$. We find that the fraction of chaotic orbits in *phase b*, that lie close to one of the three major resonances identified above, is 51% when $\alpha = 0.01$ and 62% when $\alpha = 0.03$. Weaker resonances lines (which are hard to recognise due to the sparseness of the data points) may also trap some of the chaotic orbits. This supports our conjecture that the main reason that model SA1 does not evolve in *phase b* despite the presence of a significant fraction of chaotic orbits, is that the majority of the chaotic orbits are trapped around resonances and therefore behave like regular orbits for very long times.

In Figure 13 we plot four examples of chaotic orbits in *phase b* of SA1, which illustrate how resonantly trapped or “sticky” chaotic orbits look. Each panel of four sub plots shows a single orbit plotted in two Cartesian projections (side-by-side). The top pair of sub-plots show the orbit over the first 7.5 Gyr long time segment, while the bottom pair shows the same orbit over a second 7.5 Gyr time segment. The two time segments were separated by 2.5 Gyr. For illustration we selected orbits with a range of drift parameters. The orbit in the top left panel is an example of an orbit that conforms to our notion of a chaotic orbit that explores more phase space as time progresses, and has a large drift parameter of $\log(\Delta f) = -0.51$. The top right-hand panel shows a S-tube orbit that suddenly migrates to a box orbit (this orbit has a $\log(\Delta f) = -0.65$) and was probably in the separatrix region between the S-tube and box families. Note that although the orbit in each time segment is quite different in orbital type, each looks quite regular. The bottom left-hand panel shows a chaotic orbit that is associated with the resonant boxlet (“fish”) family (this orbit has $\log(\Delta f) = -0.69$), while the bottom right-hand panel shows a box orbit that migrates to a L-tube (this orbit has a $\log(\Delta f) = -1.03$ and is formally “not chaotic” by our definition of the drift parameter, indicating that our criterion is quite conservative and may classify some weakly chaotic orbits as regular). Of the 21% of orbits in *phase b* that are chaotic ($\log(\Delta f) \geq -1$), only $\sim 5\%$ have $\log(\Delta f) \geq -0.5$. This fraction is small enough that one does not expect it to result in significant chaotic mixing.

5 DISCUSSION AND SUMMARY

It is generally believed that if a large fraction of the orbits in a self-consistent galactic potential are rendered chaotic, they will diffuse via chaotic mixing on time scales of 30 - 100 dynamical times (Merritt & Valluri 1996). Chaotic orbits in a stationary potential do not conserve any integrals of motion other than the energy E and

consequently are free to uniformly fill their allowed equipotential surface. In general, for triaxial systems, the equipotential surface is rounder than the density distribution, hence chaotic diffusion is expected to result in evolution to a more spherical shape.

Several previous numerical experiments in which a massive central baryonic component was grown in a triaxial galactic potential have shown that triaxial galaxies evolve to more spherical shape, apparently confirming the conjecture that shape evolution is driven by chaotic mixing (e.g. Merritt & Quinlan 1998; Kazantzidis et al. 2004).

Recent detailed studies of N -body simulations with controlled experiments have shown that the role of chaotic mixing may be less dramatic than conjectured by these previous studies. A study of relaxation of collisionless systems following the merger of two spherical galaxies showed that despite the fact that a large fraction of the orbits in a system undergoing violent relaxation are chaotic, the timescales for chaotic diffusion and mixing are too long for this process to play a significant role (Valluri et al. 2007). In fact, even after violent relaxation, orbits retain strong memories of their initial energies and angular momenta.

D08 argued that since a signature of chaos is extreme sensitivity to initial conditions and chaotic mixing, numerical experiments in which evolution is driven by chaotic orbits should not be reversible. These authors studied the macroscopic shapes of triaxial dark matter halos in response to the growth of a baryonic component. They concluded that much of the shape change arises from changes in the shape of individual orbits rather than significant chaotic scattering. In this paper we investigated this issue in significantly greater detail by applying the Numerical Analysis of Fundamental Frequencies (NAFF) technique that allows us to quantify the degree to which chaotic diffusion drives evolution and to identify the primary physical processes that cause halo shape change. This allows us to also identify chaotic orbits and resonant orbits and to quantify the shapes of orbits. Applying various analysis methods to orbits in four systems we confirm the conclusion reached by D08 that chaos is not an important driver of shape evolution, but do find that a significant fraction of orbits become sticky chaotic. To summarise, we showed that regardless of the original orbital composition of the triaxial halo, the halo will become more spherical following the growth of a baryonic component. We explored two different initial halos, one in which box orbits were the dominant elongated population and the other in which L-tubes dominated. Both models exhibit similar overall evolution with regard to the shapes of orbits, however in the Halo A models which were dominated by box orbits, the boxes were much more likely to change to S-tubes, whereas in the Halo B models, the dominant family of L-tubes largely retained their orbital classification. Below we list the main results of this paper:

- (i) The orbital frequencies in the three different phases ω_a , ω_b and ω_c are well correlated when the baryonic component is extended. In the more extended distributions, only a small fraction of the orbits experience significant change in their original orbital

frequencies when the baryons are evaporated. Both the magnitude of scattering in orbital frequency as well as the fraction of orbits experiencing scattering, increases as the baryonic component becomes more compact. The most significant scattering occurs for a compact point mass.

(ii) In the three models with relatively extended baryonic components, the change in orbital frequency between *phase c* and *phase a* ($\Delta\omega_{ac}$) is not correlated with orbital frequency, pericenter distance, orbital angular momentum or any other quantity we investigated. When the baryonic component is a hard point mass, however, the frequency change is greater for orbits that are deeper in the potential and therefore have both a higher initial orbital frequency and smaller pericentric radius.

(iii) The growth of a baryonic component in halo A (either disk or softened point mass) causes box orbits to be converted to S-tubes. However this change is almost completely reversible in the case of the disk, and is significantly less reversible in the case of the hard point mass. In halo B, which is dominated by L-tubes, the growth of the baryonic component causes almost no change in the orbital composition of the halo, indicating that to a large extent L-tubes are not destroyed but deformed. Even though P₁B3 is the model where we saw evidence for the greatest amount of orbit scattering by the hard central point mass, the scattering appears to mainly scatter the elongated inner L-tube orbits onto round outer L-tubes. In addition the small fraction of box orbits is also scattered to S-tubes or chaotic orbits. The significant amount of scattering seen for even centrophobic L-tube orbits shows that it is more accurate to conceptualise the scattering as arising due to the strong gradient depth and shape of the central potential, rather than as physical hard scattering by a central point mass.

(iv) In a triaxial halo orbital shapes have a bimodal distribution. The elongated orbits ($\chi_s > 0.25$) are either boxes or L-tubes. The growth of a baryonic component of any kind causes orbits of all types to become round, especially at small pericenter radii. This change in orbital shape distribution with radius is the primary cause of the change of halo shapes in response to the growth of a baryonic component. This is consistent with the findings of D08 who also found that the orbits in the models became quite round (using a different way to characterise orbital shape).

(v) The growth of a disk causes a large fraction of halo orbits to become resonantly trapped around major resonances. The three most important resonances are those associated with the 1:1 tube (thin shell) orbit that circulates about the short axis in the $x - y$ -plane, the 1:1 tube (thin shell) orbit that circulates about the long axis in the $y - z$ -plane and the 1:2 banana resonance in the $x - z$ -plane. We saw from the frequency maps that the resonant trapping of the halo particles depends both on the form of the baryonic component grown in the halo as well as on the initial orbital population of the halo.

The last of the above findings could have important implications for observational studies of the Milky Way's stellar halo. The computation expense of the orbit calculations forced us to restrict

the size of the frequency map for model SA1 to 6000 particles. This is only a tiny fraction of the particles in the original simulation. Despite the smallness of the sample, the frequency map (Fig. 12) shows a rich resonant structure which implies that the particles (either stars or dark matter) in the stellar and dark matter halos of our Galaxy, particularly those close to the plane of the disk, are likely to be associated with resonances, rather than being smoothly distributed in phase space (this is in addition to structures arising due to tidal destruction of dwarf satellites). Although significantly greater resolution is required to resolve such resonances than is currently available, this could have significant implications for detection of structures in current and upcoming surveys of the Milky Way such as SDSS-III (Segue) and in on-going direct detection experiments which search for dark matter candidates.

ACKNOWLEDGMENTS

M.V. is supported by the University of Michigan. V.P.D. thanks the University of Zürich for hospitality during part of this project. Support for one of these visits by Short Visit Grant # 2442 within the framework of the ESF Research Networking Programme entitled 'Computational Astrophysics and Cosmology' is gratefully acknowledged. Support for a visit by M.V. to the University of Central Lancashire at an early stage of this project was made possible by a Livesey Grant held by V.P.D. All simulations in this paper were carried out at the Arctic Region Supercomputing Center.

REFERENCES

- Allgood B., Flores R. A., Primack J. R., Kravtsov A. V., Wechsler R. H., Faltenbacher A., Bullock J. S., 2006, *MNRAS*, 367, 1781
 Andersen D. R., Bershady M. A., Sparke L. S., Gallagher J. S., Wilcots E. M., 2001, *ApJ*, 551, L131
 Bailin J., Steinmetz M., 2005, *ApJ*, 627, 647
 Banerjee A., Jog C. J., 2008, *ArXiv e-prints*, 806
 Bardeen J. M., Bond J. R., Kaiser N., Szalay A. S., 1986, *ApJ*, 304, 15
 Barnes E. I., Sellwood J. A., 2003, *AJ*, 125, 1164
 Barnes J., Efstathiou G., 1987, *ApJ*, 319, 575
 Bartelmann M., Steinmetz M., Weiss A., 1995, *A&A*, 297, 1
 Binney J., Spergel D., 1982, *ApJ*, 252, 308
 Binney J., Spergel D., 1984, *MNRAS*, 206, 159
 Binney J., Tremaine S., 1987, *Galactic dynamics*. Princeton, NJ, Princeton University Press, 1987, 747 p.
 Boozer A. H., 1982, *Physics of Fluids*, 25, 520
 Buote D. A., Canizares C. R., 1994, *ApJ*, 427, 86
 Buote D. A., Jeltema T. E., Canizares C. R., Garmire G. P., 2002, *ApJ*, 577, 183
 Carpintero D. D., Aguilar L. A., 1998, *MNRAS*, 298, 1
 Chirikov B. V., 1979, *Phys. Rep.*, 52, 263
 Debattista V. P., 2003, *MNRAS*, 342, 1194

- Debattista V. P., Moore B., Quinn T., Kazantzidis S., Maas R., Mayer L., Read J., Stadel J., 2008, *ApJ*, 681, 1076
- Dehnen W., 2005, *MNRAS*, 360, 892
- Diehl S., Statler T. S., 2007, *ApJ*, 668, 150
- Dubinski J., 1994, *ApJ*, 431, 617
- Dubinski J., Carlberg R. G., 1991, *ApJ*, 378, 496
- Franx M., de Zeeuw T., 1992, *ApJ*, 392, L47
- Franx M., van Gorkom J. H., de Zeeuw T., 1994, *ApJ*, 436, 642
- Frenk C. S., White S. D. M., Davis M., Efstathiou G., 1988, *ApJ*, 327, 507
- Gerhard O. E., Binney J., 1985, *MNRAS*, 216, 467
- Goodman J., Heggie D. C., Hut P., 1993, *ApJ*, 415, 715
- Habib S., Kandrup H. E., Mahon M. E., 1997, *ApJ*, 480, 155
- Hemsendorf M., Merritt D., 2002, *ApJ*, 580, 606
- Holley-Bockelmann K., Mihos J. C., Sigurdsson S., Hernquist L., Norman C., 2002, *ApJ*, 567, 817
- Huizinga J. E., van Albada T. S., 1992, *MNRAS*, 254, 677
- Iodice E., Arnaboldi M., Bournaud F., Combes F., Sparke L. S., van Driel W., Capaccioli M., 2003, *ApJ*, 585, 730
- Jing Y. P., Suto Y., 2002, *ApJ*, 574, 538
- Kandrup H. E., Sideris I. V., 2001, *Phys. Rev. E*, 64, 056209
- Kandrup H. E., Siopis C., 2003, *MNRAS*, 345, 727
- Kandrup H. E., Smith H. J., 1991, *ApJ*, 374, 255
- Kazantzidis S., Kravtsov A. V., Zentner A. R., Allgood B., Nagai D., Moore B., 2004, *ApJ*, 611, L73
- Kazantzidis S., Magorrian J., Moore B., 2004, *ApJ*, 601, 37
- Kochanek C. S., 1995, *ApJ*, 445, 559
- Koopmans L. V. E., de Bruyn A. G., Jackson N., 1998, *MNRAS*, 295, 534
- Kuijken K., Tremaine S., 1994, *ApJ*, 421, 178
- Kuo-Petravic G., Boozer A. H., Rome J. A., Fowler R. H., 1983, *Journal of Computational Physics*, 51, 261
- Laskar J., 1990, *Icarus*, 88, 266
- Laskar J., 1993, *Celestial Mechanics and Dynamical Astronomy*, 56, 191
- Lichtenberg A. J., Lieberman M. A., 1992, *Regular and chaotic motion. Applied Mathematical Sciences*, New York: Springer, 1992
- Merritt D., Quinlan G. D., 1998, *ApJ*, 498, 625
- Merritt D., Valluri M., 1996, *ApJ*, 471, 82
- Merritt D., Valluri M., 1999, *AJ*, 118, 1177
- Miller R. H., 1964, *ApJ*, 140, 250
- Moore B., Kazantzidis S., Diemand J., Stadel J., 2004, *MNRAS*, 354, 522
- Navarro J. F., Frenk C. S., White S. D. M., 1996, *ApJ*, 462, 563
- Oguri M., Lee J., Suto Y., 2003, *ApJ*, 599, 7
- Olling R. P., 1995, *AJ*, 110, 591
- Olling R. P., 1996, *AJ*, 112, 481
- Olling R. P., Merrifield M. R., 2000, *MNRAS*, 311, 361
- Papaphilippou Y., Laskar J., 1996, *A&A*, 307, 427
- Papaphilippou Y., Laskar J., 1998, *A&A*, 329, 451
- Sackett P. D., Sparke L. S., 1990, *ApJ*, 361, 408
- Schoenmakers R. H. M., Franx M., de Zeeuw P. T., 1997, *MNRAS*, 292, 349
- Schweizer F., Whitmore B. C., Rubin V. C., 1983, *AJ*, 88, 909
- Stadel J. G., 2001, Ph.D. Thesis, University of Washington
- Tremaine S., Yu Q., 2000, *MNRAS*, 319, 1
- Valluri M., Merritt D., 1998, *ApJ*, 506, 686
- Valluri M., Merritt D., 2000, in Gurzadyan V. G., Ruffini R., eds, *The Chaotic Universe, Proceedings of the Second ICRA Network Workshop, Advanced Series in Astrophysics and Cosmology*, vol.10, Edited by V. G. Gurzadyan and R. Ruffini, World Scientific, 2000, p.229 *Orbital Instability and Relaxation in Stellar Systems*. pp 229+
- Valluri M., Vass I. M., Kazantzidis S., Kravtsov A. V., Bohn C. L., 2007, *ApJ*, 658, 731

This paper has been typeset from a $\text{\TeX}/\text{\LaTeX}$ file prepared by the author.